Chapter 6

Synthesis of mesoporous cellulose matrices: Its application as a heterogeneous support for Pd NPs and study of its catalytic activity in C_{sp2}-C_{sp2} and C_{sp2}-C_{sp} cross coupling reaction

Abstract: This chapter focuses on the development of mesoporous biodegradable cellulose matrix using waste fruit peel and corresponding fabrication with *in situ* generated Pd NPs using the same fruit peel residue without use of any external chemical reducing agent. The activity of the catalytic system has been investigated in C_{sp2}-C_{sp2} and C_{sp2}-C_{sp} cross-coupling reaction. Moreover this chapter shows a significant difference in the structural morphology of cellulose matrices with conventional acid treated method and microwave assisted method.

6.1. Introduction

In the revolutionize research world, catalysis will be a central process in overcoming the engineering and scientific barriers to economically feasible routes with bio-derived and solar-mediated alternative sources for energy and chemicals. Heterogeneous catalysis in this respect has a rich history of contribution towards chemical manufacturing processes and industrial products [1,2]. They have significant advantages such as shape selectivity, surface tunability, easy separation, minimal contamination of product and facilitate energy efficient selective molecular transformations. As per the high price and limited availability of petroleum based materials, natural fibers are considered as ideal alternative candidate due to low cost, abundant, and biodegradability. Among natural fibres [3], nanofibrillar cellulose (NFC) or nanocrystalline cellulose (NCC) has received a global marketed recognition and has been applied to a broad range of fields, ranging from biomaterials, nanocomposites, and food additives to electronics, catalysis, and many more. However, in order to adjust the surface polarity or greater hydrophilic nature of NFC, various modifications have to be made [4]. Conventional production of functionalize nanocellulose involves an acid pre-treatment or enzymatic digestion by energy intensive physical techinques and or high temperature dissolution of lignocelluloses fragments [5,6]. Moreover, the morphology of the nanocellulose mainly depends on the source and the method of preparation (e.g nature and concentration of acid, acid-cellulose percentage, time and temperature of the preparative strategy). So, researchers are nowadays trying to develop newer morphological structure of cellulose apart from NFC with simple, low cost and environmentally safe methodologies

Fabrication of biodegradable materials has opened up a newer perspective in the realm of material science and for industrial evolution. Biodegradable porous materials based on natural lignocellulosic biomass have become a current interest for various research applications such as drug delivery, catalysis in synthetic applications, developments of sustainable supercapacitors etc. [7-10]. They proffer multiple advantages of low cost, lightweight, non-toxicity, and the potential in place of non-biodegradable petrochemical products [8]. Consequently, there is increasing necessity to drive biodegradable mesoporous heterogeneous materials (BHM) or nanofibrillar cellulose (NFC) from sustainable sources such as carbohydrates and fatty acids from the plant and vegetable kingdom, non-edible component of food crops such as stems, leaves,

peel and husks or cellulose from agricultural or forestry waste and from various forms of biomass [11].

With this view, herein an approach has been made towards the synthesis of mesoporous biodegradable heterogeneous solid support from waste biomass (fruit peel) and subsequent fabrication of this heterogeneous support with Pd NPs generated from its precursor peel extract. We have compared and contrast the effect of conventional acid-treated method (CAM) with green chemical-free microwave assisted method (MAM) in the synthesis of this biodegradable heterogeneous material (BHM). For the purpose, we have employed *Punica granatum* (commonly known as pomegranate) peel and modified it to mesoporous BHM or nanofibrillar cellulose (NFC) based on its mode of synthesis, and corresponding fabrication of mesoporous material with *in situ* generated Pd NPs using the pomegranate peel extract that is discarded from the peel (Figure 6.1). The synthesized BHM and Pd-anchored BHM via both the CAM and MAM approach were characterized by different analytical techniques such as SEM, EDX, TEM, Powder XRD, FT-IR, XPS, BET surface analysis and ICP-OES analysis. The Pd decorated functionalized BHM was utilized in the synthesis of biaryl and alkynyl derivative *via* Suzuki-Miyaura and Sonogashira cross-coupling reaction of heteroaryl halides and aryl boronic acid or terminal acetylene.

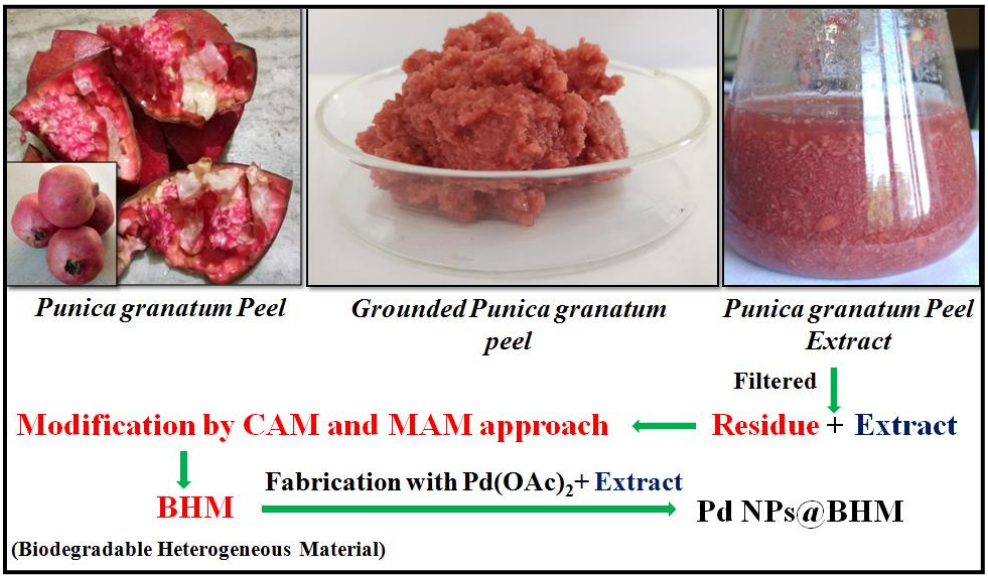

Figure: **6.1**: Pictorial presentation of pomegranate peel residue (PPR) and peel extract.

6.2. Experimental

6.2.1. Procedure for preparation of biodegradable heterogeneous material (BHM)

***Method A**: Conventional acid-treated method (CAM) of pomegranate peel, PPR(A)*:

10 g of raw pomegranate peel residue (PPR) were chopped and grounded. The mass was bleached with 7% hydrogen peroxide solution by stirring at 45°C for 2h with pH around 3-4. The PPR-H_2O_2 mixture was then neutralized by treating with 5% NaOH solution. The mixture was then filtered and washed several times with distilled water. This treatment facilitates to remove lignin and other impurities from the PPR. Finally, the bleached PPR were suspended in 50% H_2SO_4 solution and stirred at 45°C for 3h in order to break down the cellulose fibers to smaller units. The PPR(A) residue was then collected by filtration through a micro filter and washed several times with distilled water until the neutrality is maintained and then it was allowed to dry in vacuum.

***Method B**: Microwave assisted method (MAM) of pomegranate peel, PPR(M)*:

In a 100 mL two-necked microwave reactor flask, 5 g of grounded mass of PPR was mixed with 50 mL water. The mixture was then subjected to microwave irradiation with continuous stirring at 595 W (100°C) for 30 minutes with a holding time of 5 minutes. The resulting slurry was then centrifuged and washed several times with EtOH and three times with acetone. The residue was then dried under vacuum to obtain the desired BHM,[PPR(M)].

6.2.2. General procedure for fabrication of synthesized PPR(M) with Pd NPs

0.5 g of PPR(M) was mixed with $Pd(OAc)_2$ (10 wt%, 0.05 g) in a 25 mL round bottomed flask, using 10 mL of pomegranate peel extract. The mixture was allowed to stir at room temperature under N_2 atmosphere for 24h. A gradual change in color from brown to black of the $Pd(OAc)_2$/PPR solution was observed, indicating the reduction of Pd(II) ion. Thereafter the mixture was centrifuged and washed with EtOH for several times and dried under vacuum to obtain the palladium decorated PPR(M) *i.e.* Pd@PPR(M).

6.2.3. General procedure for Suzuki-Miyaura cross-coupling reaction

Aryl halide (0.5 mmol), aryl boronic acid (0.6 mmol), K_2CO_3 (1.5 mmol), Pd@PPR(M) (10 wt%) and 1:1 EtOH:H_2O (4 mL) were taken in a 25 mL round-bottom flask. The reactants were stirred at 60°C for the required time. After completion, (vide TLC) the catalyst was separated from the reaction mixture by centrifugation and the

crude reaction mixture was extracted with ethyl acetate (3×10 mL). The resultant organic phase was washed with brine (2×10 mL) and dried over anhydrous Na_2SO_4, filtered and evaporated under reduced pressure and purified by column chromatography using ethyl acetate and n-hexane as eluent. The products were characterized by ^1H and ^{13}C NMR spectroscopic analyses.

For recycling experiments, the reaction mixture was centrifuged and the residue catalyst was washed four times with excess water and then with ethyl acetate in sequence. The resultant catalyst was dried under vacuum and subjected to consequent run.

6.2.4. General procedure for Sonagashira cross-coupling reaction

(A) Sonagashira cross-coupling reaction of aryl iodides: Aryl iodides (0.5 mmol), terminal acetylene (0.6 mmol), base (1.5 mmol), Pd@PPR(M) (10 wt%) and EtOH (4 mL) were taken in a 25 mL round-bottom flask. The reactants were stirred at 70 ^oC under aerobic condition. After completion (vide TLC) the catalyst was separated from the reaction mixture by centrifugation and the crude reaction mixture was extracted with ethyl acetate (3×10 mL) and dried over anhydrous Na_2SO_4. The products were purified by column chromatography using n-hexane and ethyl acetate as eluent. The products were identified by ^1H and ^{13}C NMR spectroscopic analyses.

(B) Sonagashira cross-coupling reaction of aryl bromides: Aryl bromides (0.5 mmol), terminal acetylene (0.6 mmol), base (1.75 mmol), Pd@PPR(M) (10 wt%) and DMF (4 mL) were taken in a 100 mL two-necked round-bottom flask. The air inside the round bottom flask was replaced with nitrogen (balloon) by three vacuum/nitrogen cycles. The mixture was then subjected to stirring at 90 $^{\circ}C$ for specific time interval and the progress of the reaction was monitored by TLC. After completion, the catalyst was separated from the reaction mixture by centrifugation and the crude reaction mixture was extracted with ethyl acetate (3×10 mL) and dried over anhydrous Na_2SO_4. The products were purified by column chromatography using n-hexane and ethyl acetate as eluent. The products were identified by ^1H and ^{13}C NMR spectroscopic analyses.

For recycling experiments of Sonogashira reaction, similar procedure as Suzuki-Miyaura cross-coupling reaction was followed.

6.3. Results and Discussion

6.3.1. Characterization of catalysts

At the onset the morphology of the developed BHM via CAM and MAM approach were identified by TEM analysis (Figure 6.2).

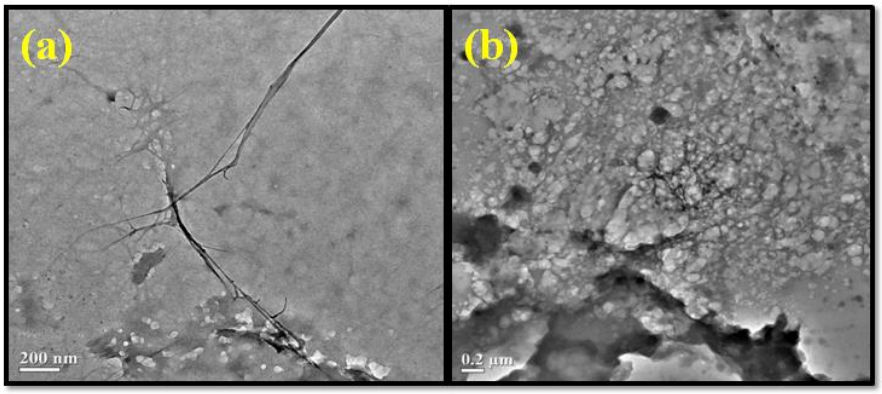

Figure 6.2: TEM images of **(a)** PPR(A) and **(b)** PPR(M).

TEM analysis reveals different surface anatomy of PPR based on its mode of preparation by acid treated method (CAM) and microwave assisted method (MAM). CAM strategy for development of PPR shows a fibrous network (Figure 6.2 a) of cellulose matrix. However, the MAM strategy for development of biodegradable heterogeneous material or PPR(M) shows the formation of highly porous structure (Figure 6.2 b).

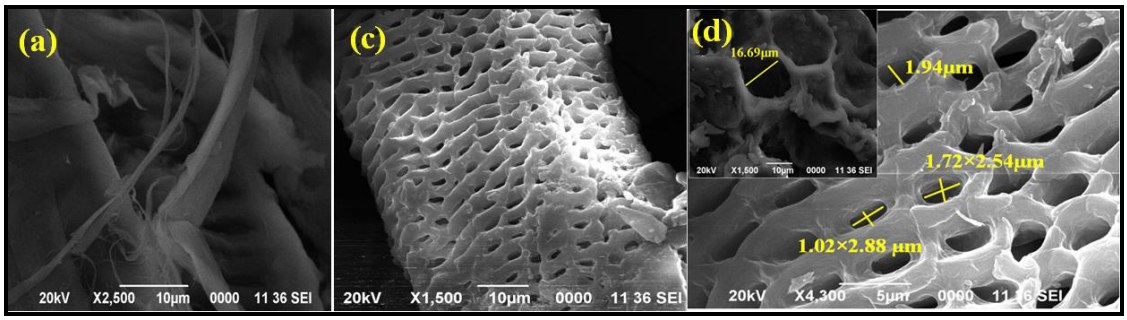

Figure 6.3: SEM images of **(a)** PPR(A) **(c) and (d)** PPR(M).

The morphological structure was further confirmed from scanning electron microscopy (SEM) studies which shows a distinct fibrous cellulose network for CAM methodology (Figure 6.3 a) and a distorted honeycomb like highly porous structure for MAM approach for development of BHM, with pore dimension between 1-2 µm or some

larger pore diameter with 16.69 µm (Figure 6.3 b and c). As a result, this mesoporous nature of MAM develop PPR(M), serves to be an attractive heterogeneous material for incorporation of metal into it. So, considering the greener alternative route in contrast to acid treated method for development of biodegradable heterogeneous material, we further utilized this PPR(M) in incorporation of Pd NPs into its mesopores and corresponding catalytic study in Suzuki-Miyaura and Sonogashira cross-coupling reaction.

At the onset, the formation of the Pd NPs from the PPR extract was confirmed by comparing its FTIR spectrum with $Pd(OAc)_2$ (Figure 6.4 a, b). The disappearance of characteristic vibrational peak in Figure 6.4 b observed at 691 cm^{-1} due to Pd-O of $Pd(OAc)_2$ (Figure 6.4 a), reveals the reduction of Pd(II) to Pd(0). The *in situ* generation of Pd NPs and its corresponding incorporation in the PPR(M) was confirmed by FTIR spectrum shown in Figure 6.4 c and d. The broad vibrational band around 3400 cm^{-1} corresponds to O-H stretching of strongly tetrahedrally-bonded water patches. Medium to strong intensity vibration around 2923 cm^{-1} is due to $\nu_{C\text{-}H}$ stretching of methylene group. The similarity of IR-vibrational peaks of PPR(M) (Figure 6.4c) and Pd@PPR(M) (Figure 6.2 d) signifies strong interaction between the Pd NPs and PPR (M). Additionally, the absence of distinct peak at 691 cm^{-1} due to Pd-O in Figure 6.2 d reveals the generation of Pd(0) species and subsequent incorporation of the same in PPR(M).

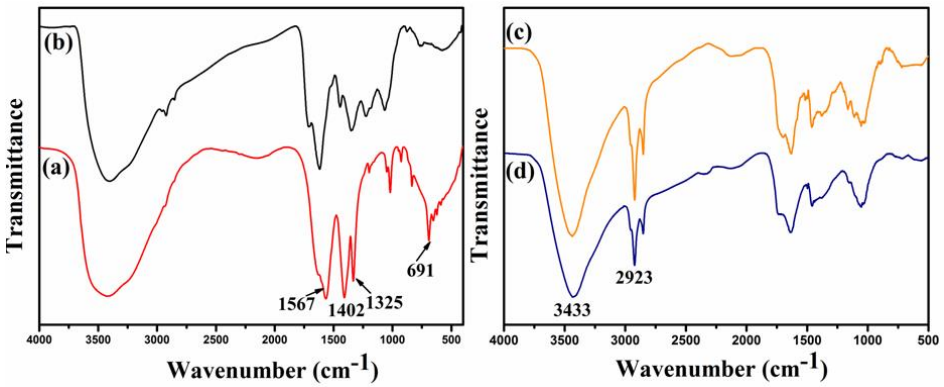

Figure: **6.4**: FTIR spectra of **(a)** $Pd(OAc)_2$, **(b)** Pd NP, **(c)** PPR(M) and **(d)** Pd@PPR(M).

Powder XRD analysis as shown in Figure 6.5 I, reveals the incorporation of Pd NPs onto PPR(M) pores. Figure 6.5 Ia represents the powder XRD pattern of PPR(M) . The broad diffraction peak at 2θ between 15-30º is attributed to the amorphous carbon structures with C (002) reflection [12,13]. Thus the peak at 2θ value 21.8 in Fig 6.5 Ia, is

due to the presence of carbon backbone of PPR(M). Further Fig 6.5 Ib shows the additional peaks for Pd NPs with 2θ value 39.9°, 46.3° and 67.5° corresponding (111), (200) and (220) reflections respectively. The Pd NPs shows the formation of the face-centered cubic (fcc) lattice system of the palladium nanostructure which matches well with the standard XRD database (JCPDS card no. 89-4897). The presence of Pd in the PPR(M) framework was further confirmed from the EDX analysis, which shows the presence of Pd along with C and O.

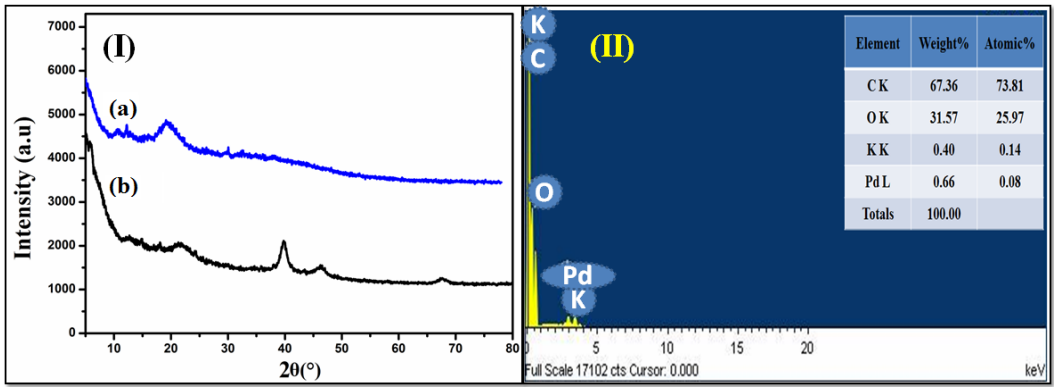

Figure 6.5: **(I)** Powder XRD spectra of **(a)** PPR(M) and **(b)** Pd@PPR(M) **(II)** EDX analysis of Pd@PPR(M).

Since EDX analysis reveals the presence of oxygen along with carbon, we further studied the chemical state of Pd at Pd@PPR(M) by XPS analysis (Figure 6.6). The survey scan spectrum of Pd@PPR(M) shows the presence of Pd along with higher intensity peak of carbon and oxygen (Figure 6.6 a). The high resolution peak fitting Pd3d spectrum for Pd@PPR(M) reveals the presence of four distinct peaks at 335.1 eV, 337.7 eV, 340.4 eV and 343 eV, which belongs to the Pd(0), Pd(II), Pd(0) and Pd(II), respectively attributed to the $Pd3d_{5/2}$ and $Pd3d_{3/2}$ spin-orbit peaks of Pd NPs (Figure 6.6 b) [14]. Further, the high-resolution C1s and O1s spectrum as shown in Figure 6.6 c and d also confirmed the presence of PdO and Pd particle in the carbon backbone.

Further evidence of incorporation of Pd NPs in the pores of Pd@PPR(M) was obtained from its morphological study by TEM and SEM analysis. The fabrication of MAM developed PPR with *in situ* generated Pd NPs shows a high distribution of Pd(0) particles in the porous network of PPR(M) (Figure 6.7 a). The Pd NPs incorporated in PPR(M) are spherical in shape with a particle size ranging from 5-11 nm (Figure 6.7 b). HRTEM image of Pd@PPR(M) shows the presence of crystal planes with the lattice spacing of 0.23 nm corresponding to (111) reflection of face centre cubic (fcc) Pd NPs

(Figure 6.7 c). The corresponding SAED pattern of Pd NPs shows four well-resolved rings corresponding to crystallographic planes (111), (200), (220) and (311) of Pd NPs (inset in Figure 6.7c).

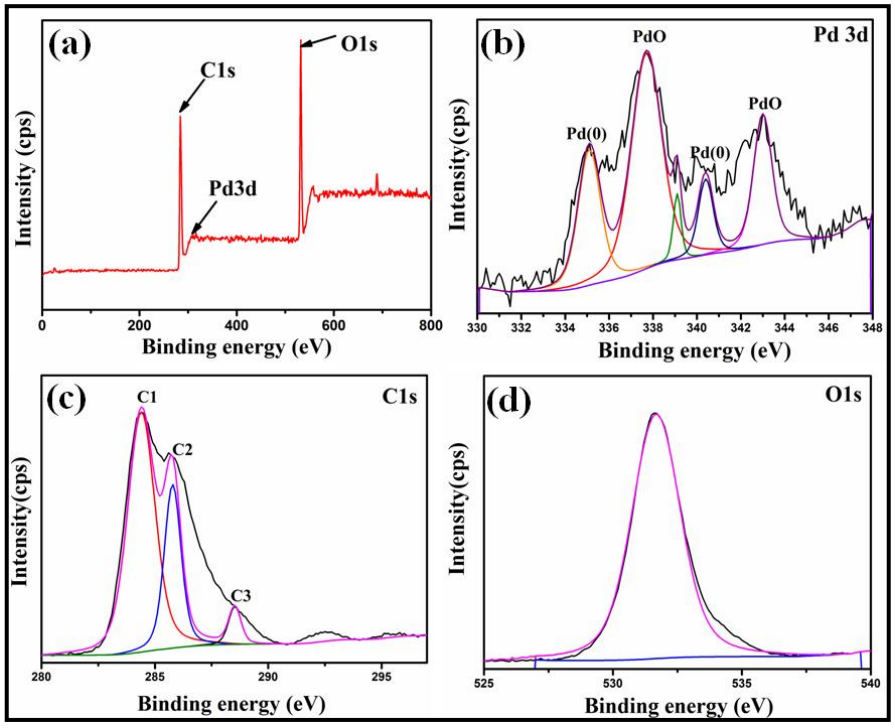

Figure 6.6: **(a)** XPS survey spectrum, **(b, c** and **d)** high-resolution Pd3d, C1s and O1s spectrum respectively of Pd@PPR(M)

Figure 6.7: TEM images **(a** and **b)** and **(c)** HRTEM image of Pd@PPR(M), inset in **(c)** SAED pattern of Pd@PPR(M)

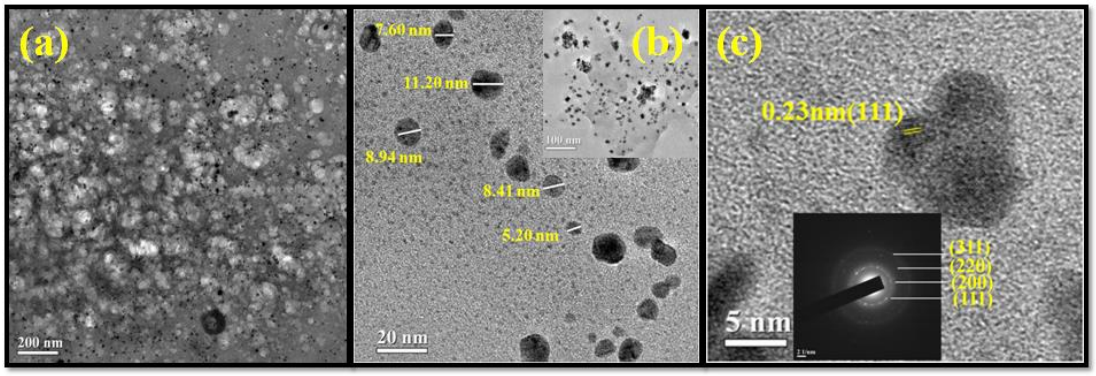

Again, Figure 6.8 a-d shows the SEM images of Pd@PPR(M), it was clearly observed that the Pd NPs are distributed over the porous PPR(M) surface and decreases the pore volume as a result of incorporation onto the pores. This characteristic of

PPR(M) and Pd@PPR(M) is in accordance with the BET measurements of the samples (Figure 6.9).

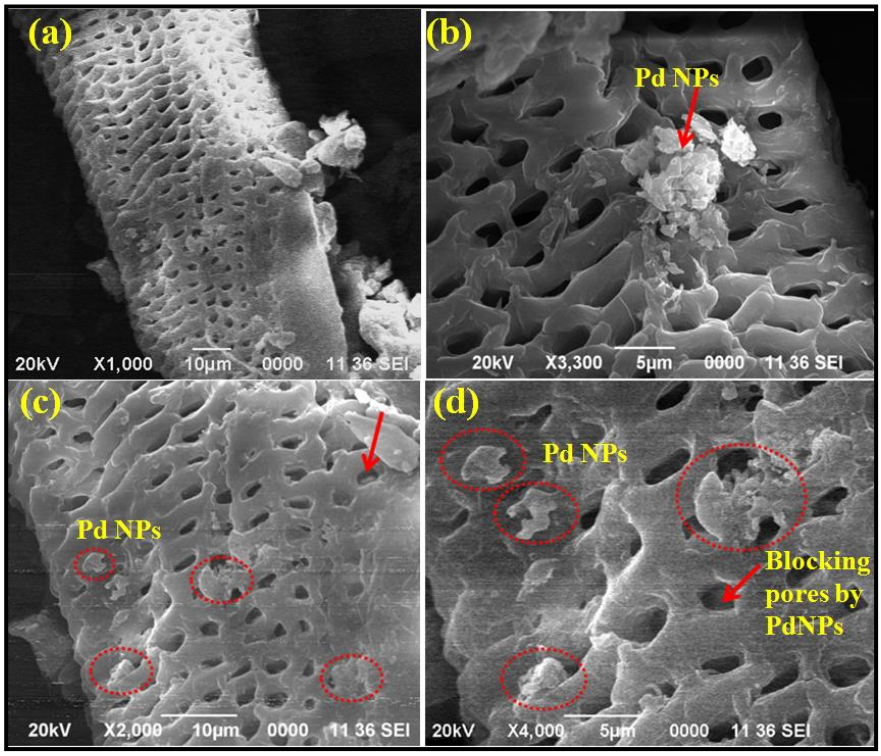

Figure 6.8: (**a**, **b**, **c** and **d**) are the SEM images of Pd@PPR(M)

BET surface analysis technique based on N_2 adsorption-desorption isotherm analysis of PPR(M) before and after fabrication with Pd NPs provides complete details on the specific surface area and porosity of the samples. The sorption isotherms in Figure 6.9 I and II are of type IV according to the IUPAC classification [15-18], which involves adsorption on mesoporous adsorbents with strong adsorbate-adsorbent interaction. Figure 6.9 I shows a combination of H1 and H3 hysteresis loop, which is a characteristic of mesoporous materials. BET investigation of the of PPR(M) (Figure 6.9 I) provides a surface area of about 48.607 m^2/g which is slightly greater than BET surface area of Pd@PPR(M) (Figure 6.9 II) with 46.432 m^2/g. This is due to the pore blockage of mesoporous PPR(M) with Pd NPs which as a result decreases its surface area resulting in strong interaction between PPR(M) and Pd NPs. Moreover the isotherm in Fig 6.9 II shows a H2 hysteresis loop which reveals its narrower pore network compared to precursor PPR(M) (Fig 6.9 I). Consequently, the incorporation of Pd NPs and mesoporosity of the PPR(M) was confirmed by its BJH pore size distribution which

indicates that the pore size of the porous PPR(M) is 11.941 nm and decreases to 8.284 nm after incorporation of Pd NPs onto it.

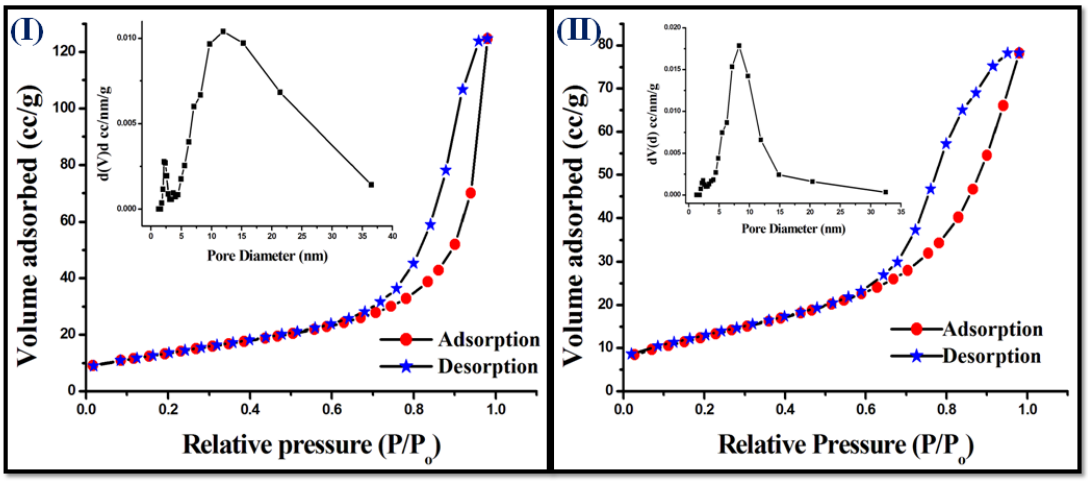

Figure 6.9: N_2 adsorption/desorption isotherm of **(I)** PPR(M) **(II)** Pd@PPR(M), and inset in **(I)** and **(II)** are the pore size distribution curves.

MAM approach for development of PPR(M) follows the greener perspectives as it does not utilize any chemical reagents for its modification. Additionally, in the *in situ* generation of Pd NPs, no external conventional reducing agents were used. Thus MAM approach for synthesis of BHM is a highly green synthetic mode since it does not discard any portion of PPR and as such does not lead to any waste deposition. Further in order to reveal the incorporation of Pd NPs in PPR(M), ICP-OES analysis of Pd@PPR(M) was performed and it was found that 0.01mg (0.02 wt%) Pd NPs was incorporated in the mesoporous of PPR(M).

6.3.2. Application of catalysts in Suzuki-Miyaura cross-coupling reaction

6.3.2.1. Optimization of catalytic system for Suzuki-Miyaura coupling reaction

Considering the greener reaction pathway and mesoporous nature of Pd@PPR(M), further catalytic study was done using microwave derived Pd@PPR(M) The efficiency of the catalytic system is initially assessed in Suzuki-Miyaura cross-coupling reaction of 4-bromoanisole and phenylboronic acid using 10 wt% of catalyst using different bases and solvents at room temperature (Table 6.1). Among the different bases studied, K_2CO_3 was found to be the most effective in terms of reaction efficiency and time (Table 6.1, entries 1-7). We have also performed the reaction in different solvent systems such as H_2O, EtOH, CH_3CN, *i*-PrOH and THF (Table 6.1, entries 7-11). Among all, H_2O:EtOH

(1:1) system serves to be an efficient reaction medium and delivers the desired product within shorter reaction time (Table 6.1, entry 1). The catalytic activity using only H_2O and EtOH provides comparatively lower conversion (Table 6.1, entries 7 and 8). This is due to the weaker interaction of heterogeneous catalytic surface and reaction substrates, since the catalytic system requires biphasic condition for better correlation of the reaction species. Again, the reaction was examined by lowering the amount of Pd catalyst, but the reaction yield significantly decreases to 75% (Table 6.1, entry 12).

Table 6.1: Optimization of reaction conditions for Suzuki-Miyaura reaction [a]

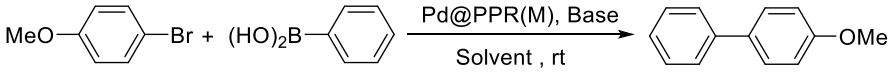

Entry	Base (mmol)	Solvent (mL)	Time (h)	Yield (%) [b]
1	K_2CO_3	H_2O:EtOH (1:1)	1	95
2	Na_2CO_3	H_2O:EtOH (1:1)	1	90
3	Cs_2CO_3	H_2O:EtOH (1:1)	1	92
4	NaOH	H_2O:EtOH (1:1)	4	50
5	KOH	H_2O:EtOH (1:1)	4	65
6	Et_3N	H_2O:EtOH (1:1)	4	40
7	K_2CO_3	EtOH	4	70
8	K_2CO_3	H_2O	8	60
9	K_2CO_3	CH_3CN	4	60
10	K_2CO_3	*i*-PrOH	8	40
11	K_2CO_3	THF	8	40
12	K_2CO_3	H_2O:EtOH (1:1)	4	75 [c]

[a]Reaction conditions: 4-bromoanisole (0.5 mmol), phenylboronic acid (0.6 mmol), base (1.5 mmol), solvent (4 mL), Pd@PPR(M) (10 wt%, 0.00003 mmol Pd), rt. [b] Isolated yields [c] Pd@PPR(M) (5 wt%)

6.3.2.2. Substrate scope for Suzuki-Miyaura coupling reaction

Considering the optimized condition obtained from Table 6.1, we next studied the potential of Pd@PPR(M) for electronically diverse aryl bromides (Table 6.2). It is seen that both electron withdrawing and electron donating aryl bromides provide excellent yield of cross-coupling product (Table 6.2, 3a-f). We then tried to investigate the cross-coupling of heteroaryl bromides with different substituted aryl boronic acid. Interestingly, excellent cross-coupling was achieved at 60°C although a comparative longer reaction time was required (Table 6.2, 3g-l). However coupling of 3-bromopyridine with *p*-Cl and *p*-OMe phenylboronic acid results relatively lower yield of cross-coupling product (Table 6.2, 3m and 3n). Coupling of 3-bromoquinoline with

phenylboronic acid and 4-methoxyphenylboronic acid delivers moderate yield of desired biaryl derivative (Table 6.2, 3o and 3p). We have examined the effect of catalytic system on the coupling of heteroaryl boronic acid with aryl bromides. Excellent catalytic efficiency was observed using 2-methoxypyridine-5-boronic acid as coupling partner with electron withdrawing aryl bromides (Table 6.2, 3q and 3r). However, coupling with electron donating 4-bromoanisole results in lower conversion of cross-coupling reaction (Table 6.2, 3s). Additionally, cross-coupling of heteroaryl bromides with heteroaryl boronic acid was also investigated. 70% of the desired biaryl derivative was obtained by performing the reaction at 80°C (Table 6.2, 3t).

Table 6.2: Substrate scope for Suzuki-Miyaura reaction [a]

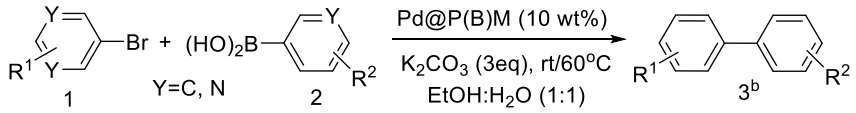

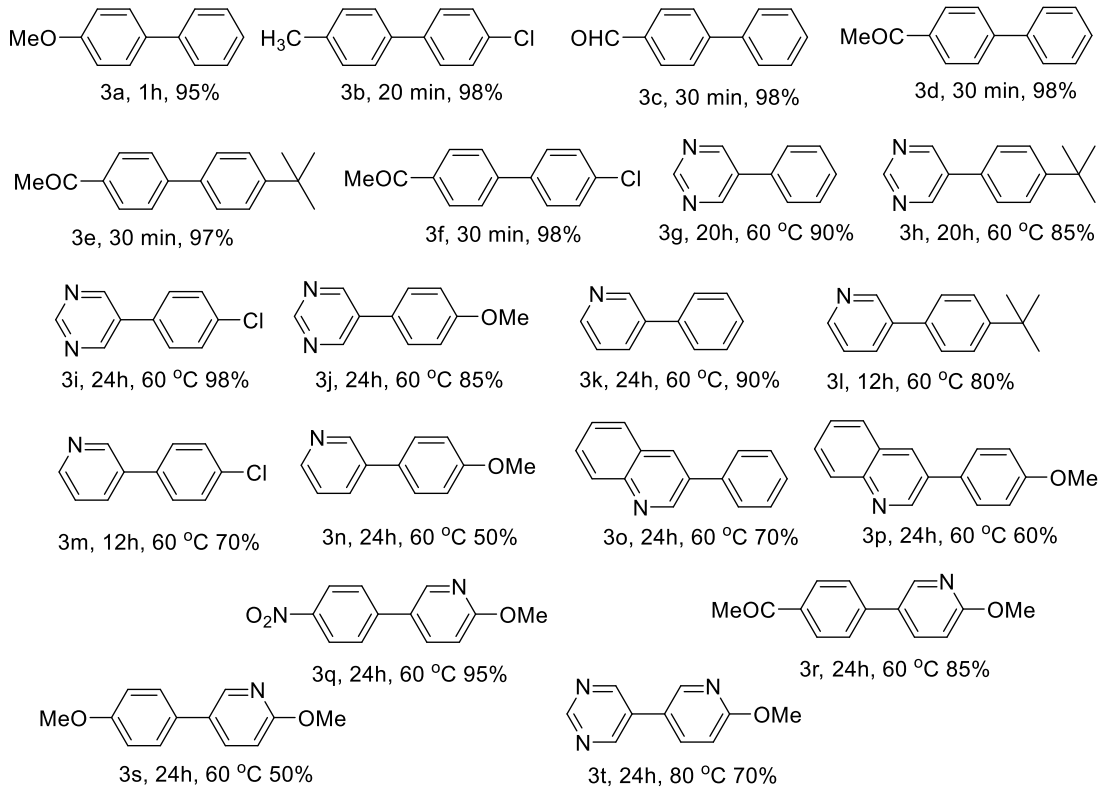

[a] Reaction conditions: aryl bromide (0.5 mmol), aryl boronic acid (0.6 mmol), Pd@PPR(M) (10 wt%), K_2CO_3 (1.5 mmol), EtOH:H_2O (1:1) (4 mL) [b] Isolated yields

6.3.2.3. Recyclability of Pd@PPR(M) in Suzuki-Miyaura reaction

The reusability of a catalyst is an important factor as per green principles and for commercial applications. And since the major challenge of a heterogeneous catalyst is its

ability to reuse. So, we have performed the the recyclability test of Pd@PPR(M) using 4-bromoanisole and phenylboronic acid as the coupling partners using the optimized reaction condition. The catalytic system could be reused upto 5th consequtive cycle without any significant loss in its catalytic activity (Figure 6.10).

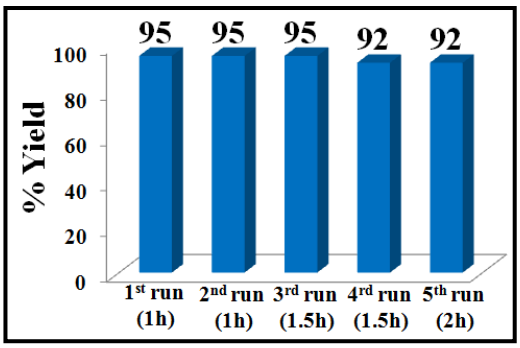

Figure 6.10: Reusability of Pd@PPR(M) in Suzuki-Miyaura cross-coupling reaction.

TEM image of the recovered catalyst after 5th cycle shows distribution of spherical Pd NPs in the mesopores of PPR(M) (Figure 6.11a).

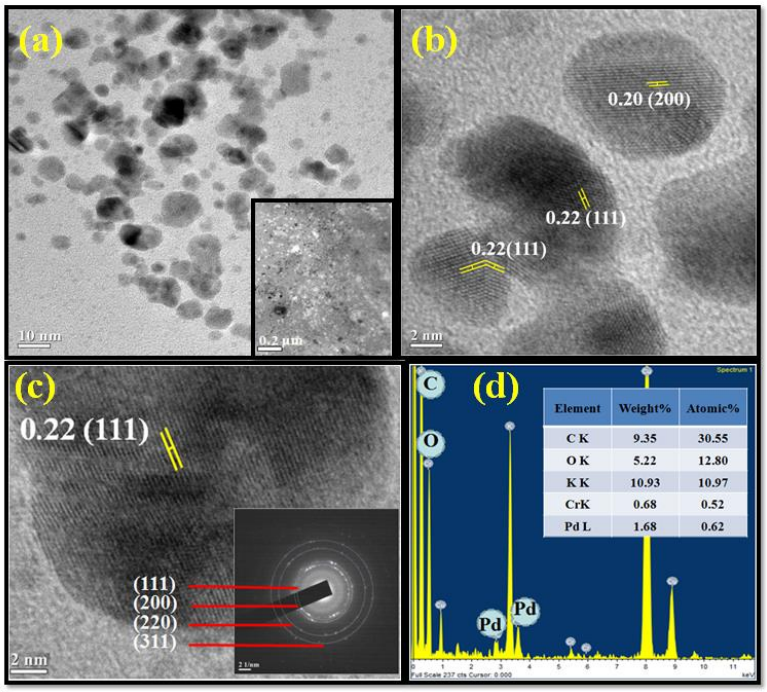

Figure 6.11: (a), (b), (c) TEM and HRTEM images of Pd@PPR(M) after 5th reuse, inset in (c) is the SAED pattern of Pd@PPR(M) and (d) EDX analysis of reused Pd@PPR(M)

Further HRTEM images also reveals the presence of crystal planes with the lattice spacing of 0.22 nm and 0.20 nm corresponding to (111) and (200) reflection respectively

of face centre cubic (fcc) Pd NPs (Figure 6.11 b and c). SAED pattern does not show any difference from the fresh Pd@PPR(M), and represents well resolved crystalline fringes corresponding to (111), (200), (220) and (311) crystallographic planes of Pd NPs (Figure 6.11c, inset). EDX analysis of the recovered catalyst also reveals the presence of palladium along with carbon, oxygen and trace of other elements (Figure 6.11d).

6.3.3. Application of catalysts in Sonogashira cross-coupling reaction

6.3.3.1. Optimization of catalytic system for Sonogashira coupling reaction

Considering the similar reaction condition we next tried to investigate the catalytic activity of Pd@PPR(M) in the Sonogashira cross-coupling of heteroaryl iodide (3-iodopyridine) and phenylacetylene (Table 6.3).

Table 6.3: Optimization of reaction conditions for Sonogashira coupling reaction [a]

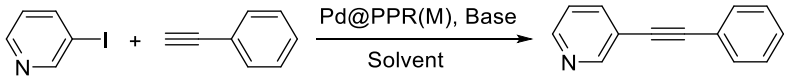

Entry	Base (mmol)	Solvent (mL)	Time (h)	Yield (%)[b]
1	K_2CO_3	H_2O(1):EtOH (1)	12	50 [c]
2	K_2CO_3	EtOH	12	70 [c]
3	K_2CO_3	H_2O(0.5)/EtOH(4)	7	90
4	Na_2CO_3	H_2O(0.5)/EtOH(4)	12	40
5	Cs_2CO_3	H_2O(0.5)/EtOH(4)	7	90
6	NaOH	H_2O(0.5)/EtOH(4)	7	70
7	Et_3N	H_2O(0.5)/EtOH(4)	12	40
8	K_2CO_3	H_2O(4)	12	30
9	K_2CO_3	THF(4)	8	40
10	K_2CO_3	H_2O(0.5)/EtOH(4)	12	50 [d]

[a] Reaction conditions: 3-iodopyridine (0.5 mmol), phenylacetylene (0.75 mmol), base (1.5 mmol), Pd@PPR(M) (10 wt%), 70 °C [b] Isolated yields [c] rt [d] Pd@PPR(M) (5 wt%)

At first, we were able to isolate minimum amount of cross-coupling product using the standardised reaction condition of Suzuki-Miyaura coupling (Table 6.3, entry 1). However use of alcoholic solvents such as ethanol gave comparative better result (Table 6.3, entry 2). Thereafter we have performed the reaction by increasing the temperature to 70 °C. Excellent amount of desired product was obtained using 0.5 mL H_2O with 4 mL EtOH at 70 °C (Table 6.3, entry 3). The reaction was examined for different bases such as Na_2CO_3, Cs_2CO_3, NaOH, Et_3N and different solvents like H_2O and THF, but among all K_2CO_3 and Cs_2CO_3 in H_2O (0.5 mL)/EtOH (4 mL) provides excellent cross-coupling

(Table 6.3, entries 4-9). On lowering the amount of Pd@PPR(M), the reaction yield significantly decreases to 50% (Table 6.3, entry 10).

We then tried to extend the scope of the present catalytic system towards coupling of aryl bromides and phenylacetylene. For that, initially we have investigated the cross-coupling reaction between 4-bromonitrobenzene and phenylacetylene using 10 wt% Pd@PPR(M) and K_2CO_3 (3eq) in H_2O(0.5 mL)/EtOH (4mL) at 70 °C (Table 6.4, entry 1). It was observed that the cross-coupling reaction does not proceed effectively. Since C-Br activation is difficult compared to C-I, the reaction require high temperature to achieve efficient cross-coupling product. Thereafter the reaction was performed by increasing the temperature to 90°C using DMF as the reaction medium. Appreciable yield of cross-coupling product was observed, but relatively greater homocoupling of phenylacetylene was obtained (Table 6.4, entry 2). Consequently, with an aim to minimize the Glaser type homocoupling of phenylacetylene, we have carried out the reaction under nitrogen atmosphere. Interestingly, 80% of the desired diarylalkyne was obtained under N_2 atmosphere at 90°C in DMF (Table 6.4, entry 3). Since base plays an important role in activating the terminal alkyne, increasing the amount of K_2CO_3 to 3.5 eq, slightly greater efficiency was achieved (Table 6.4, entry 4). Decreasing the temperature to 70°C, lower conversion of cross-coupling product was obtained (Table 6.4, entry 5).

Table 6.4: Optimization of reaction conditions for Sonogashira coupling of aryl bromides and phenylacetylene [a]

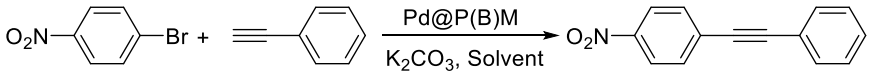

Entry	Solvent(mL)	Temperature (°C)	Yield (%) [b]
1	H_2O(0.5)/EtOH	70	40
2	DMF	90	70
3	DMF	90 (N_2 atm)	80
4	DMF	90 (N_2 atm)	85 [c]
5	DMF	70 (N_2 atm)	50

[a] Reaction conditions: 4-bromonitrobenzene (0.5 mmol), phenylacetylene (0.75 mmol), Pd@PPR(M) (10 wt%), Solvent (4 mL), K_2CO_3(1.5 mmol, 3 eq) [b] Isolated yields [c] K_2CO_3 (3.5 eq)

6.3.3.2. Substrate scope for Sonogashira coupling reaction

Since heteroaryl derivatives are key structural intermediates in medicinal chemistry and biological active compounds including antifungal, anti-inflammatory, antibacterial, antioxidant etc, they provide rapid exchange of research in the field of organic, analytical, and medicinal chemistry. With this view, we have focused on the Sonogashira cross-coupling of heteroaryl bromides and phenylacetylene using the standardized reaction condition mentioned in Table 6.4. The synthesized Pd@PPR(M) provides excellent cross-coupling for different heteroaryl bromides and phenylacetylene. 3-bromopyridine and 5-bromopyrimidine in all cases provides good to excellent yield of hetero-diarylalkyne (Table 6.5, 6a-c and 6e, 6f). However, a comparative lower amount of desired product was obtained using 3-bromoquinoline as the coupling partner (Table 6.5, 6d, 6g).

Table 6.5: Substrate scope for Sonogashira coupling of heteroaryl bromides and terminal acetylene [a]

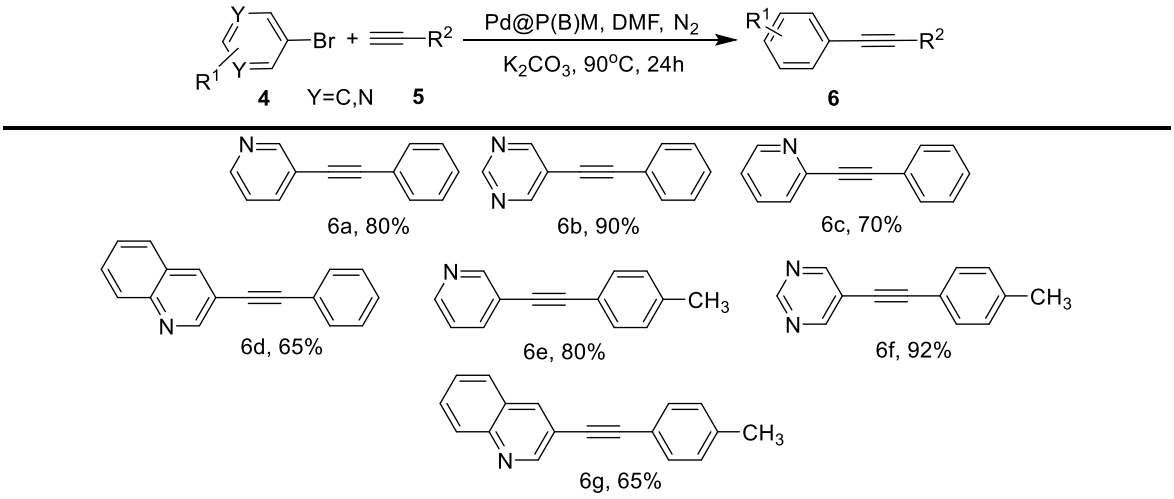

[a] Reaction conditions: aryl bromide (0.5 mmol), terminal acetylene (0.6 mmol), Pd@PPR(M) (10 wt%), K_2CO_3 (1.75 mmol), DMF (4 mL) [b] Isolated yields

6.3.3.3. Recyclability of Pd@PPR(M) in Sonogashira cross-coupling reaction

The recyclability of the Pd@PPR(M) in Sonogashira cross-coupling reaction was investigated using 4-bromonitrobenzene and phenylacetylene using the standardized reaction condition. The catalytic system could be reused up to 3rd cycle without any significant loss in its catalytic activity. However, in the consecutive 4th run comparatively some losses in activity was observed (Figure 6.12). The gradual decrease in yield from 82 to 70% might be due to physical loss of the catalyst in the separation

process. Otherwise, the catalyst [Pd@PPR(M)] shows excellent efficiency, stability and reusability indicating the effective incorporation of Pd particles in the modified PPR (BHM). In order to confirm the extent of interaction of Pd NPs in the pores of PPR(M) we have performed the hot filtration test with the catalyst.

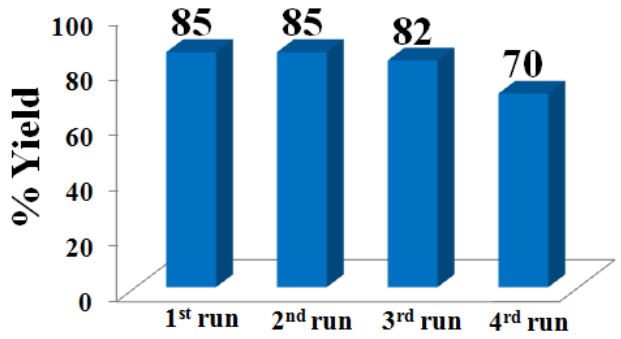

Figure 6.12: Reusability of Pd@PPR(M) in Sonogashira cross-coupling reaction.

6.3.4. Hot filtration test

To identify the heterogeneous nature of the Pd@PPR(M), we have performed the hot filtration test considering Suzuki-Miyaura cross-coupling reaction of 4-bromoanisole and phenylboronic acid with the standard optimized reaction condition and the progress of the reaction was monitored by TLC. After 50% conversion (30 min); the reaction mixture was filtered. The reaction was continued with the filtrate for additional 30 mins. But no increase in cross-coupling product formation was observed. This proves that Pd is strongly incorporated in the pores of PPR(M).

6.4. Conclusions

In summary, we have developed a novel strategy for development of mesoporous biodegradable heterogeneous material using waste peel of fruit. Moreover, we have compared and contrast the synthetic methodology with conventional methodology for development of cellulose matrices. Additionally fabrication of the developed biodegradable heterogeneous material (by MAM) was done by *in situ* immobilization of Pd NPs and its catalytic activity was investigated in Suzuki-Miyaura and Sonogashira cross-coupling reaction. The catalytic system can be utilized in the Suzuki-Miyaura coupling of heteroaryl halides with heteroaryl boronic acid and Sonogashira coupling of heteroaryl bromides and terminal acetylene.

6.5. Analytical data of the synthesized biaryl derivatives

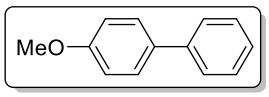

4-Methoxybiphenyl: (Table 6.2, 3a): White Solid, m.p. 81-83 °C, **^{1}H NMR (400 MHz, $CDCl_3$):** δ 7.58-7.50 (m, 4H), 7.42 (t, *J* = 7.7 Hz, 2H), 7.30 (t, 1H, *J* = 7.1 Hz), 6.98 (d, 2H, *J* = 8.5 Hz), 3.85 (s, 3H).ppm. **^{13}C NMR (100 MHz, $CDCl_3$):** δ 159.2, 140.9, 133.8, 128.8, 128.2, 126.8, 126.7, 114.2, 55.4 ppm.

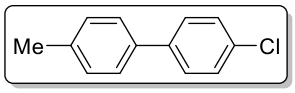

4-Chloro-4′-methylbiphenyl: (Table 6.2, 3b): White Solid, m.p. 122-124 °C, **^{1}H NMR (400 MHz, $CDCl_3$):** 7.50-7.37 (m, 6H), 7.25-7.23 (m, 2H), 2.39 (s, 3H) ppm. **^{13}C NMR (100 MHz, $CDCl_3$):** δ 139.6, 137.5, 137.1, 133.1, 129.6, 129.1, 128.9, 128.2, 21.1 ppm.

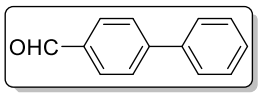

4-Formylbiphenyl: (Table 6.2, 3c): White Solid, m.p. 57-59 °C, **^{1}H NMR (400 MHz, $CDCl_3$):** δ 10.05 (s, 1H), 7.97-7.93 (m, 2H), 7.77-7.72 (m, 2H), 7.66-7.61 (m, 2H), 7.50-7.39 (m, 3H) ppm. **^{13}C NMR (100 MHz, $CDCl_3$):** δ 192.0, 147.3, 139.8, 135.2, 130.3, 129.1, 128.5, 127.7, 127.4 ppm.

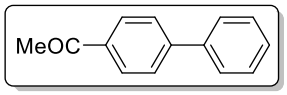

4-Acetylbiphenyl: (Table 6.2, 3d): White Solid, m.p. 118-120 °C, **^{1}H NMR (400 MHz, $CDCl_3$):** δ 8.09-7.96 (m, 2H), 7.72-7.66 (m, 2H), 7.65-7.57 (m, 2H), 7.50-7.34 (m, 3H), 2.63 (s, 3H).ppm. **^{13}C NMR (100 MHz, $CDCl_3$):** δ 197.8, 145.8, 139.9, 135.9, 129.0, 128.9, 128.3, 127.3, 127.1, 26.7 ppm.

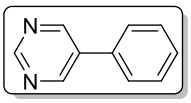

5-Phenylpyrimidine: (Table 6.2, 3g): Colourless liquid**, ^{1}H NMR (400 MHz, $CDCl_3$):** δ 9.16 (s, 1H), 8.90 (s, 2H), 7.56-7.40 (m, 5H) ppm. **^{13}C NMR (100 MHz, $CDCl_3$):** δ 157.5, 154.9, 134.3, 134.2, 129.5, 129.0, 127.0 ppm.

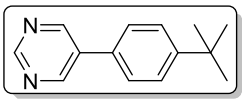

5-(4'-*tert*-Butyl)phenylpyrimidine: (Table 6.2, 3h): Pale yellow oil**, ^{1}H NMR (400 MHz, $CDCl_3$):** δ 9.17 (s, 1H), 8.94 (s, 2H), 7.53-7.52 (m, 4H), 1.36 (s, 9H) ppm. **^{13}C NMR (100 MHz, $CDCl_3$):** δ 157.3, 154.8, 152.4, 134.2, 131.3, 126.7, 126.5, 34.8, 31.3ppm.

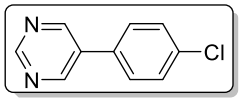

5-(4'-Chloro)phenylpyrimidine: (Table 6.2, 3i): White Solid, **^{1}H NMR (400 MHz, $CDCl_3$):** δ 9.17 (s, 1H), 8.88 (s, 2H), 7.53-7.37 (m, 4H) ppm. **^{13}C NMR (100 MHz, $CDCl_3$):** δ 157.7, 154.8, 135.4, 133.3, 132.7, 129.7, 128.3 ppm.

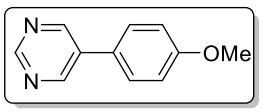

5-(4'-Methoxy)phenylpyrimidine: (Table 6.2, 3j): Pale yellow oil, **^{1}H NMR (400 MHz, $CDCl_3$):** δ 9.13 (s, 1H), 8.89 (s, 2H), 7.79-6.37 (m, 4H), 3.85 (s, 3H) ppm. **^{13}C NMR (100 MHz, $CDCl_3$):** δ 160.5, 156.9, 154.5, 134.0, 128.2, 126.5, 115.0, 55.5 ppm.

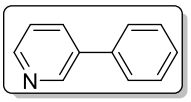

3-Phenylpyridine: (Table 6.2, 3k): Colourless liquid**, ^{1}H NMR (400 MHz, $CDCl_3$):** δ 8.69-8.68 (m, 2H), 8.53-8.51 (m, 2H), 7.86-7.83 (m, 2H), 7.24-7.18 (m, 3H) ppm. **^{13}C NMR (100 MHz, $CDCl_3$):** δ 156.6, 150.6, 147.4, 139.3, 129.6, 125.1, 121.2, 120.1, 115.5 ppm.

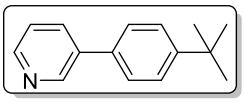

3-(4'-*tert*-Butyl)phenylpyridine: (Table 6.2, 3l): Pale yellow oil**, ^{1}H NMR (400 MHz, $CDCl_3$):** δ 8.84 (s, 1H), 8.56 (dd, 1H, *J* = 4.9, 1.6 Hz), 7.89 (ddd, 1H, *J* = 7.9, 2.2, 1.7 Hz), 7.60-7.12 (m, 5H).ppm. **^{13}C NMR (100 MHz, $CDCl_3$):** δ 151.5, 147.5, 136.9, 134.8, 126.9, 126.8, 126.2, 126.1, 123.8, 34.7, 31.3 ppm.

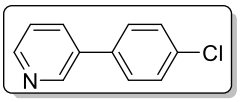

3-(4'-Chloro)phenylpyridine: (Table 6.2, 3m): Colourless Solid, m.p. 155-157 °C, **^{1}H NMR (400 MHz, $CDCl_3$):** δ 8.81 (s, 1H), 8.59 (dd, 1H, *J* = 4.8, 1.4 Hz), 7.86 (ddd, 1H, *J* = 3.9, 2.8, 1.7 Hz), 7.60-7.30 (m, 5H).ppm. **^{13}C NMR (100 MHz, $CDCl_3$):** δ 148.1, 147.5, 136.0, 134.8, 134.6, 129.4, 129.3, 128.4, 123.9 ppm.

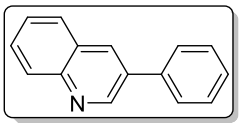

3-Phenylquinoline: (Table 6.2, 3o): Pale yellow Solid**,** 52-55 °C, **^{1}H NMR (400 MHz, $CDCl_3$):** δ 9.18 (s, 1H), 8.29 (s, 1H), 8.14 (d, 1H, *J* = 8.5 Hz), 7.87 (d, 1H, *J* = 8.2 Hz), 7.79-7.67 (m, 3H), 7.61-7.38 (m, 4H) ppm. **^{13}C NMR (100 MHz, $CDCl_3$):** δ 150.0, 147.4, 137.9, 133.9, 133.3, 129.4, 129.3, 129.2, 128.2, 128.0, 127.5, 127.0 ppm.

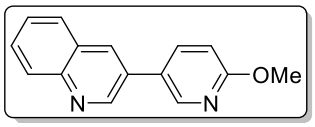

3-(6-Methoxypyridin-3-yl)quinoline: (Table 6.2, 3p): Pale yellow Solid, **^{1}H NMR (400 MHz, $CDCl_3$):** δ 9.08 (s, 1H), 8.48 (s, 1H), 8.19 (d, 1H, *J* = 2.1 Hz), 8.11 (d, 1H, *J* = 8.4 Hz), 7.91-7.79 (m, 2H), 7.69 (ddd, 1H, *J* = 8.4, 6.9, 1.4 Hz), 7.59-7.49 (m, 1H), 6.86 (d, 1H, *J* = 8.6 Hz), 3.98 (s, 3H).ppm. **^{13}C NMR (100 MHz, $CDCl_3$):** δ 164.1, 149.3, 147.3, 145.4, 137.5, 132.7, 130.8, 129.5, 129.2, 127.9, 127.2, 126.9, 111.4, 55.7 ppm.

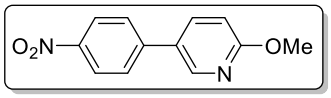

2-Methoxy-5-(4'-nitro)phenylpyridine: (Table 6.2, 3q): Yellow Solid**, ^{1}H NMR (400 MHz, $CDCl_3$):** δ 8.30-8.26 (m, 2H), 7.82-7.79 (m, 1H), 7.71-7.64 (m, 2H), 6.86-6.79 (m, 2H), 3.95 (s, 3H) ppm. **^{13}C NMR (100 MHz, $CDCl_3$):** δ 164.6, 163.7, 145.6, 144.5, 137.4, 137.1, 127.2, 127.0, 124.4, 111.4, 53.8 ppm.

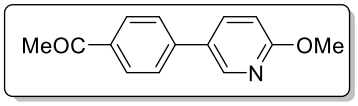

1-(4-(6-Methoxypyridin-3-yl)phenylethan-1-one: (Table 6.2, 3r): White Solid**, ^{1}H NMR (400 MHz, $CDCl_3$):** 8.42-8.41 (dd, 1H, *J* = 2.7 Hz), 8.03-8.00 (m, 2H), 7.81 (ddd, 1H, *J* = 8.7, 2.7, 1.4 Hz), 7.62-

7.59 (m, 2H), 6.84-6.81 (m, 1H), 3.97 (s, 3H), 2.62 (s, 3H).ppm. **^{13}C NMR (100 MHz, $CDCl_3$):** δ 197.6, 179.6, 164.2, 145.4, 142.5, 137.4, 129.1, 128.8, 126.6, 111.1, 53.7, 26.7 ppm.

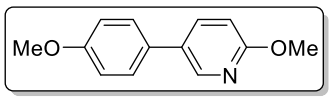

2-Methoxy-5-(4'-methoxy)phenylpyridine: (Table 6.2, 3s): Yellow Solid**, ^{1}H NMR (400 MHz, $CDCl_3$):** δ 8.34 (d, 1H, *J* = 2.5 Hz), 7.78-7.65 (m, 1H), 7.48-7.35 (m, 2H), 7.01-6.88 (m, 2H), 6.78 (d, 1H, *J* = 8.6 Hz, 1H), 3.96 (s, 3H), 3.82 (s, 3H) ppm. **^{13}C NMR (100 MHz, $CDCl_3$):** δ 163.2, 159.2, 144.5, 137.3, 129.1, 128.8, 127.8, 114.5, 110.7, 55.4, 53.6 ppm.

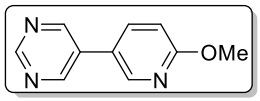

5-(6'-Methoxypyridin-3-yl)pyrimidine: (Table 6.2, 3t): Pale yellow Solid**, ^{1}H NMR (400 MHz, $CDCl_3$):** δ 9.19 (s, 1H), 8.89 (s, 2H), 8.37 (dd, *J* = 2.8, 0.7 Hz, 1H), 7.77 (dd, *J* = 8.7, 2.7 Hz, 1H), 6.88 (dd, *J* = 8.7, 0.8 Hz, 1H), 3.98 (s, 3H).ppm. **^{13}C NMR (100 MHz, $CDCl_3$):** δ 164.7, 157.5, 154.4, 145.2, 137.0, 131.6, 123.3, 111.8, 53.8 ppm.

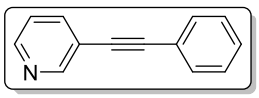

3-(Phenylethynyl)pyridine (Table 6.3, entry 3): Yellow liquid, **^{1}H NMR (400 MHz, $CDCl_3$):** δ 8.74 (s, 1H), 8.50 (d, 1H, *J* = 4.7 Hz), 7.84-7.67 (m, 1H), 7.61-7.41 (m, 2H), 7.27 (m, 4H) ppm.**^{13}C NMR (100 MHz, $CDCl_3$):** δ 152.0, 148.3, 138.7, 131.7, 129.8, 128.5, 123.2, 122.5, 120.6, 92.9, 85.9 ppm.

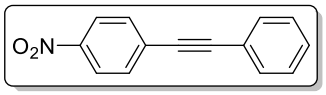

1-Nitro-4-(2-phenylethynyl)benzene (Table 6.4, entry 4): Yellow Solid**, ^{1}H NMR (400 MHz, $CDCl_3$):** δ 8.23-8.16 (m, 2H), 7.69-7.60 (m, 2H), 7.55 (m, 2H), 7.43-7.33 (m, 3H) ppm. **^{13}C NMR (100 MHz, $CDCl_3$):** δ 147.0, 132.3, 131.9, 130.3, 129.3, 128.6, 123.7, 122.1, 94.8, 87.6 ppm

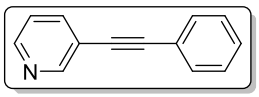

3-(Phenylethynyl)pyridine (Table 6.5, 6a): Yellow liquid, **^{1}H NMR (400 MHz, $CDCl_3$):** δ 8.81-8.73 (m, 1H), 8.52 (dd, 1H, *J* = 4.9, 1.6 Hz), 7.86-7.71 (m, 1H), 7.58-7.46 (m, 2H), 7.39-7.17 (m, 4H).ppm.**^{13}C NMR (100 MHz, $CDCl_3$):** δ 152.0, 148.3, 138.7, 131.7, 129.8, 128.5, 123.2, 122.5, 120.6, 92.9, 85.9 ppm.

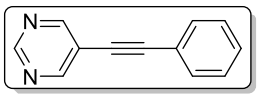

5-(Phenylethynyl)pyrimidine (Table 6.5, 6b): Yellow liquid, **^{1}H NMR (400 MHz, $CDCl_3$):** δ 9.12 (s, 1H), 8.83 (s, 2H), 7.53 (m, 2H), 7.43-7.29 (m, 3H).ppm.**^{13}C NMR (100 MHz, $CDCl_3$):** δ 158.6, 156.7, 131.8, 129.4, 128.6, 121.8, 120.0, 96.4, 82.3 ppm.

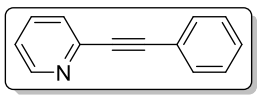

2-(Phenylethynyl)pyridine (Table 6.5, 6c): Yellow oil, **^{1}H NMR (400 MHz, $CDCl_3$):** δ 8.60 (ddd, 1H, *J* = 4.9, 1.7, 0.9 Hz), 7.66 (td, 1H, *J* = 7.7, 1.8 Hz), 7.58 (dd, 2H, *J* = 6.7, 3.0 Hz), 7.51 (dt, 1H, *J* = 7.9, 1.1 Hz),

7.40-7.30 (m, 3H), 7.28-7.15 (m, 1H).ppm.**^{13}C NMR (100 MHz, $CDCl_3$):** δ 150.1, 143.5, 136.2, 132.1, 129.0, 128.4, 127.2, 122.8, 122.3, 92.6, 89.3 ppm.

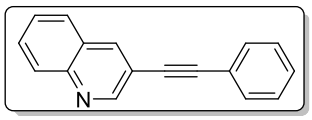

3-(Phenylethynyl)quinoline (Table 6.5, 6d): Yellow solid, **^{1}H NMR (400 MHz, $CDCl_3$):** δ 8.99 (s, 1H), 8.32-8.27 (m, 1H), 8.10 (d, 1H, *J* = 8.4 Hz), 7.84-7.65 (m, 2H), 7.63-7.51 (m, 3H), 7.43-7.30 (m, 3H).ppm.**^{13}C NMR (100 MHz, $CDCl_3$):** δ 152.2, 146.8, 138.3, 131.8, 130.1, 129.4, 128.9, 128.5, 127.6, 127.3, 122.6, 117.5, 92.7, 86.7 ppm.

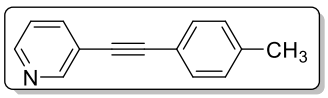

3-(Phenylethynyl)pyridine (Table 6.5, 6e): White Solid, m.p. 50–51 °C, **^{1}H NMR (400 MHz, $CDCl_3$):** δ 8.73 (s, 1H), 8.51 (d, 1H, *J* = 4.5 Hz), 7.82-7.66 (m, 1H), 7.42 (d, *J* = 7.8 Hz, 2H), 7.28-7.21 (m, 1H), 7.19-7.11 (m, 2H), 2.35 (s, 3H).ppm.**^{13}C NMR (100 MHz, $CDCl_3$):** δ 152.2, 148.4, 139.1, 138.4, 131.6, 129.3, 123.1, 119.4, 92.9, 85.9, 21.6 ppm.

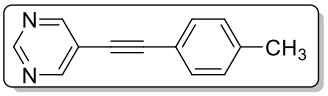

5-(*p*-tolylethynyl)pyrimidine (Table 6.5, 6f): White solid, **^{1}H NMR (400 MHz, $CDCl_3$):** δ 9.11 (s, 1H), 8.82 (s, 2H), 7.48-7.36 (m, 2H), 7.17 (d, 2H, *J* = 8.0 Hz), 2.36 (s, 3H) ppm.**^{13}C NMR (100 MHz, $CDCl_3$):** δ 158.6, 156.5, 139.8, 131.7, 129.4, 120.2, 118.7, 96.7, 81.8, 21.6 ppm.

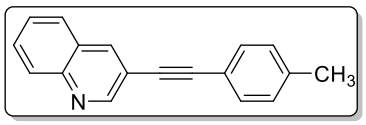

3-(*p*-tolylethynyl)quinoline (Table 6.5, 6g): Yellow solid, **^{1}H NMR (400 MHz, $CDCl_3$):** δ 8.99 (d, 1H, *J* = 2.0 Hz), 8.29 (d, 1H, *J* = 1.9 Hz), 8.10 (d, 1H, *J* = 8.5 Hz), 7.83-7.76 (m, 1H), 7.71 (ddd, 1H, *J* = 8.4, 6.9, 1.4 Hz), 7.60-7.42 (m, 3H), 7.21-7.15 (m, 2H), 2.38 (s, 3H).ppm.**^{13}C NMR (100 MHz, $CDCl_3$):** δ 152.1, 146.8, 139.2, 138.3, 131.7, 130.1, 129.3, 129.2, 127.6, 127.4, 119.5, 117.8, 93.0, 86.0 ppm.

^{1}H and ^{13}C NMR spectra of 3-(4'-*tert*-Butyl)phenylpyrimidine

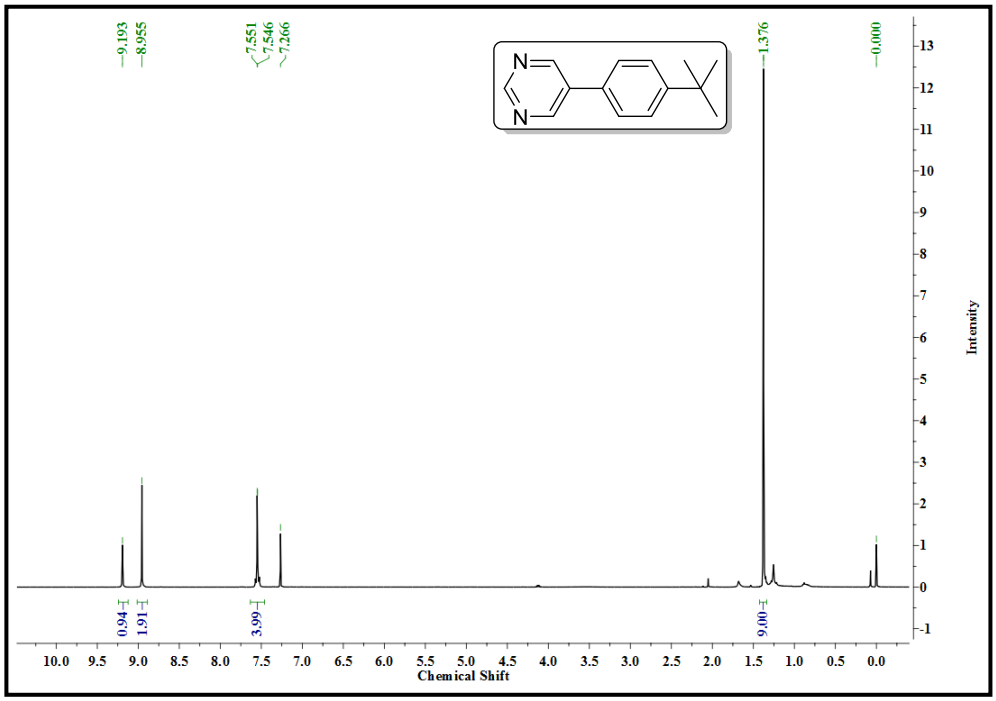

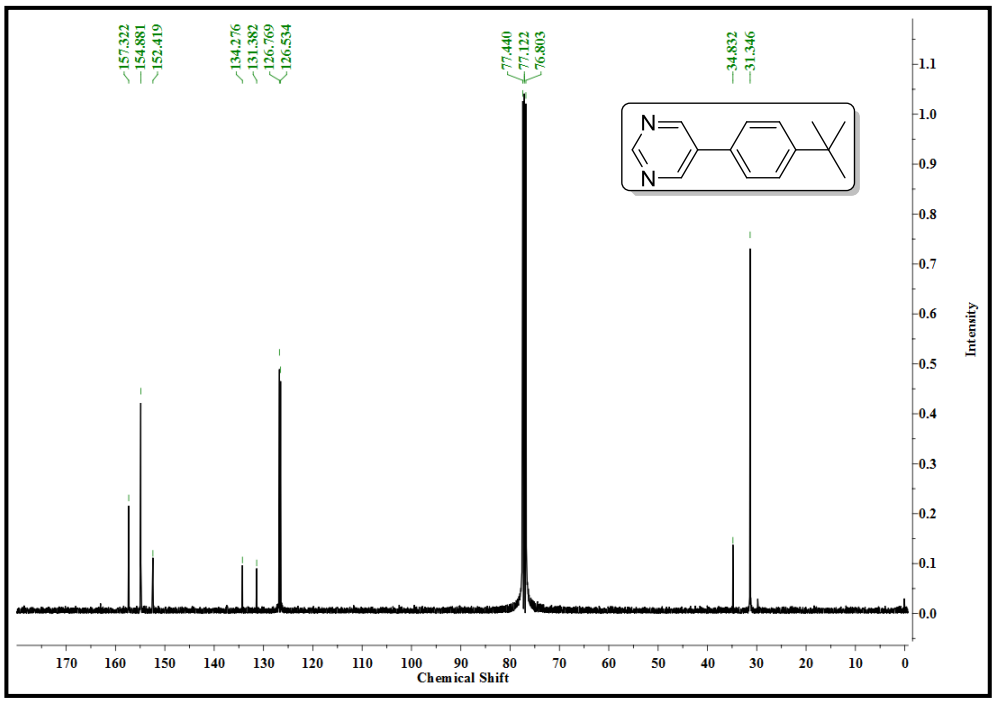

^{1}H and ^{13}C NMR spectra of 5-(*p*-tolylethynyl)pyrimidine

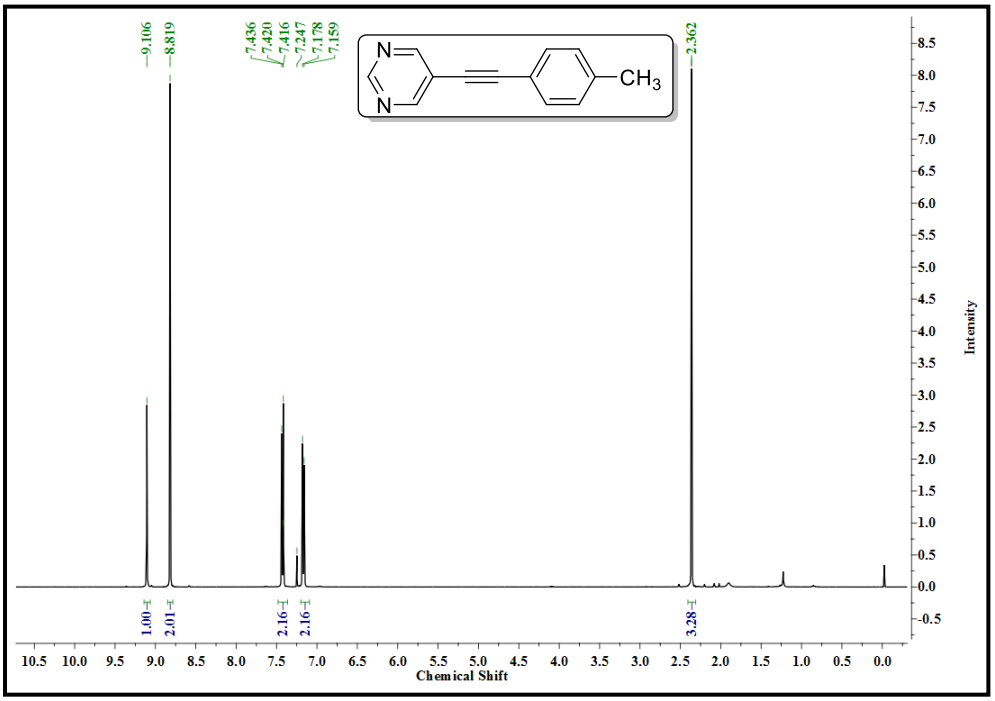

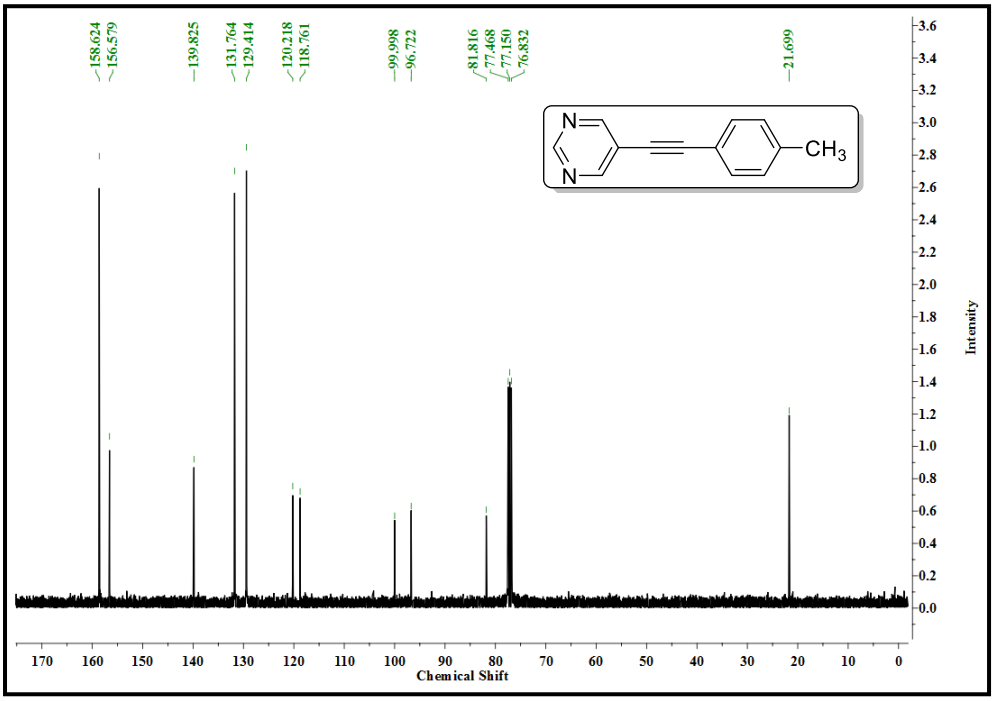

6.6. References

[1] Thomas, J. M. The societal significance of catalysis and the growing practical importance of single-site heterogeneous catalysts. *Proceedings of the Royal Society A: Mathematical, Physical and Engineering Science*, 468(2143):1884-1903, 2012.

[2] Somorjai, G. A., Frei, H., and Park, J. Y. Advancing the frontiers in nanocatalysis, biointerfaces, and renewable energy conversion by innovations of surface techniques. *Journal of the American Chemical Society*, 131(46):16589-16605, 2009.

[3] Alila, S., Besbes, I., Vilar, M. R., Mutjé, P., and Boufi, S. Non-woody plants as raw materials for production of microfibrillated cellulose (MFC): A comparative study. *Industrial Crops and Products*, 41:250-259, 2013.

[4] Siró, I. and Plackett, D. Microfibrillated cellulose and new nanocomposite materials: A review. *Cellulose*, 17(3):459-494, 2010.

[5] Barua, S., Das, G., Aidew, L., Buragohain, A. K., and Karak, N. Copper–Copper oxide coated nanofibrillar cellulose: A promising biomaterial. *RSC Advances*, 3(35):14997-15004, 2013.

[6] Rebouillat, S. and Pla, F. State of the art manufacturing and engineering of nanocellulose: A review of available data and industrial applications. *Journal of Biomaterials and Nanobiotechnology*, 4(2):165-188, 2013.

[7] Udenni Gunathilake, T. M. S., Ching, Y. C., Ching, K. Y., Chuah, C. H., and Abdullah, L. C. Biomedical and microbiological applications of bio-based porous materials: A review. *Polymers*, 9(5):160, 2017.

[8] Xu, A. R., Chen, L., Guo, X., Xiao, Z., and Liu, R. Biodegradable lignocellulosic porous materials: fabrication, characterization and its application in water processing. *International Journal of Biological Macromolecules*, 115:846-852, 2018.

[9] Gupta, G. K., De, S., Franco, A., Balu, A. M., and Luque, R. Sustainable biomaterials: Current trends, challenges and applications. *Molecules*, 21(1):48, 2016.

[10] Jiao, F., Edberg, J., Zhao, D., Puzinas, S., Khan, Z. U., Mäkie, P., Naderi, A., Lindström, T., Odén, M., Engquist, I., Berggren, M., and Crispin, X. Nanofibrillated cellulose-based electrolyte and electrode for paper-based supercapacitors. *Advanced Sustainable Systems*, 2(1):1700121, 2018.

[11] Lee, A. F., Bennett, J. A., Manayil, J. C., and Wilson, K. heterogeneous catalysis for sustainable biodiesel production *via* esterification and transesterification. *Chemical Society Reviews*, 43(22):7887-7916, 2014.

[12] Liu, X. Y., Huang, M., Ma, H. L., Zhang, Z. Q., Gao, J. M., Zhu, Y. L., Han, X. J., and Guo, X. Y. Preparation of a carbon-based solid acid catalyst by sulfonating activated carbon in a chemical reduction process. *Molecules*, 15(10):7188-7196, 2010.

[13] Jadhav, S. N., Kumbhar, A. S., Rode, C. V., and Salunkhe, R. S. Ligand-free Pd catalyzed cross-coupling reactions in an aqueous hydrotropic medium. *Green Chemistry*, 18(7):1898-1911, 2016.

[14] Sá, S., Gawande, M. B., Velhinho, A., Veiga, J. P., Bundaleski, N., Trigueiro, J., Tolstogouzov, A., Teodoro, O. M. N. D., Zboril, R., Varma, R. S., and Branco, P. S. magnetically recyclable magnetite–palladium (nanocat-Fe–Pd) nanocatalyst for the Buchwald–Hartwig reaction. *Green Chemistry*, 16(7):3494-3500, 2014.

[15] Sing, K. S. reporting physisorption data for gas/solid systems with special reference to the determination of surface area and porosity (Recommendations 1984). *Pure and Applied Chemistry*, 57(4):603-619, 1985.

[16] Kruk, M., and Jaroniec, M. Gas Adsorption characterization of ordered organic−inorganic nanocomposite materials. *Chemistry of Materials*, 13(10):3169-3183, 2001.

[17] Xu, C., and Hedin, N. Synthesis of microporous organic polymers with high CO_2-over-N_2 selectivity and CO_2 adsorption. *Journal of Materials Chemistry A*, 1(10):3406-3414, 2013.

[18] Sehaqui, H., Zhou, Q., and Berglund, L. A. High-porosity aerogels of high specific surface area prepared from nanofibrillated cellulose (NFC). *Composites Science and Technology*, 71(13):1593-1599, 2011.